Nanoscale

Accepted Manuscript

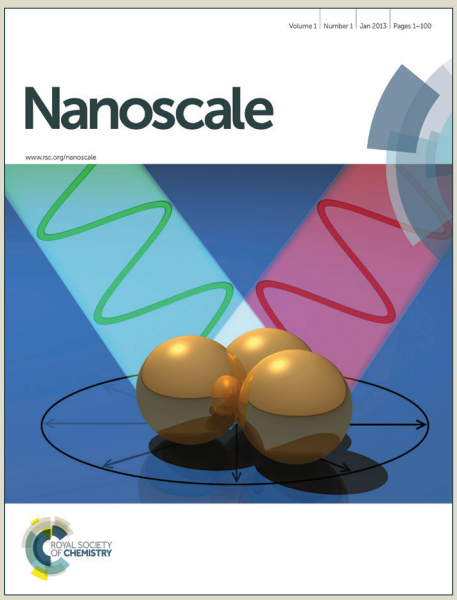

ROYAL SOCIETY OF CHEMISTRY

www.rsc.org/nanoscale

Diels-Alder functionalized carbon nanotubes for bone tissue engineering: *in vitro/in vivo* biocompatibility and biodegradability

D. Mata[a*], M. Amaral[a,b], A.J.S. Fernandes[b], B. Colaço[c], A. Gama[c], M.C. Paiva[d], P.S. Gomes[e], R.F. Silva[a], M.H. Fernandes[e]

[a]CICECO, Materials and Ceramic Eng. Dept., Univ. of Aveiro, 3810-193 Aveiro ,Portugal

[b]I3N, Physics Dept., Univ. of Aveiro, 3810-193 Aveiro ,Portugal

[c]Dept. of Veterinary Sciences, Center for the Study of Animal Sciences (CECA), ECAV, Univ. of Trás-os-Montes e Alto Douro, 5000-801 Vila Real, Portugal

[d]Institute for Polymers and Composites/I3N, Univ. of Minho, 4800-058 Guimarães, Portugal

[e]Laboratory for Bone Metabolism and Regeneration, Faculty of Dental Medicine, Univ. of Porto, 4200-393 Porto, Portugal

[*]Corresponding author

Fax: +351 234 425 300
E-mail address: diogomata@ua.pt (D. Mata)

Abstract

The risk-benefit balance for carbon nanotubes (CNTs) dictates their clinical fate. To take a step forward in this crossroad it is compulsory to modulate the CNT *in vivo* biocompatibility and biodegradability via e. g. chemical functionalization.

CNT membranes were functionalised combining a Diels-Alder cycloaddition reaction to generate cyclohexene ($-C_6H_{10}$) followed by a mild oxidisation to yield carboxylic acid groups (-COOH). *In vitro* proliferation and osteogenic differentiation of human osteoblastic cells were maximized on functionalized CNT membranes (*p,f*-CNTs). The *in vivo* subcutaneously implanted materials showed higher biological reactivity, thus inducing a slighter intense inflammatory response relatively to non-functionalized CNT membranes (*p*-CNTs), but still showing a reduced cytotoxicity profile. Moreover, the *in vivo* biodegradation of CNTs was superior for *p,f*-CNTs membranes, likely mediated by oxidation-induced myeloperoxidase (MPO) in neutrophils and macrophages inflammatory milieus. This put evidences for the biodegradability faculty of functionalized CNTs, which potentially avoids long-term tissue accumulation and triggering of acute toxicity.

On the whole, the proposed Diels-Alder functionalization was accounted for the improved CNT biological response as referred to biocompatibility and biodegradability profiles. Therefore, CNTs can be considered to be used in bone tissue engineering without noteworthy toxicological threats.

Introduction

Pioneering solutions based on carbon nanotubes - single-walled (SWCNTs) and multi-walled (MWCNTs) - have been widely explored to endorse relevant breakthroughs in bone tissue engineering upmost demands of scaffolding, drug delivering, cell tracking and sensing, and *in situ* control of cell proliferation and differentiation[1-3]. Moreover, the outstanding idea that all of these functionalities could be accumulated in a unique multifunctional CNT-based smart bone graft triggered a huge excitement in the bone tissue engineering field.

Despite the enthusiasm for CNT-engineered biomedical products, the potential CNT toxicological risks made, so far, some of their applications unrealistic to clinic. CNT toxicity is still a controversial topic, while some studies have shown biocompatibility with cells and tissues [4], others have demonstrate their toxic effect [5]. This discrepancy is explained by variations across research groups in the physical-chemical characteristics of the CNTs used (structure, morphology, purity, functionalization) and in the adopted experimental protocols, namely, preparation methods (concentration, dispersion) and route of administration.[6] Indeed, up to now, studies clearly show that metal impurities, morphology, hydrophobicity and non-biodegradability dictate the *in vitro* and *in vivo* toxicological profiles of CNTs [6, 7]. Transition-metal impurities used in CNT production processes induce cell toxicity by acting as catalyst to oxidative stress [8]. Also, the CNT morphology is crucial for the success of the clearance, either through urinary and/or lymphatic mechanisms [9-11]. Small pristine (i.e. non-functionalized) CNTs have their potential toxicity highly depressed by having the ability to be excreted through *fenestrae* of the organs and by being engulfed and digested by phagocytes [10, 11]. Yet, purifying and shortening pristine CNTs just solve part of their toxicological risks.

Chemical functionalization becomes essential to reduce hydrophobicity and biopersistency [12]. Chemical charging of CNTs restricts the formation of big agglomerates and increases the CNT mobility in physiological serums and ultimately avoid their accumulation into cell, tissues and organs [10]. Furthermore, covalent type functionalization might help to design biodegradable and bioresorbable CNTs under *in vivo* scenarios of material accumulation and retention [12]. *In vitro* studies revealed that the level and type of the chemical groups covalently bonded to CNTs dictate their cleavage/oxidation rate in simulated oxidative phagolysosome media containing acidic hydrolase enzymes (lysozymes), hydrogen peroxide and superoxide anions [13, 14]. The carboxylic group (-COOH) is the most efficient to produce biodegradable CNTs due to the uppermost level of induced damage, originating active sites at two neighboring C atoms due to C-C bond breaking [14]. Carboxylic groups are commonly added to highly reactive ends and at defect sites of CNTs by means of strong acidic oxidation procedures [15]. Notwithstanding, the intrinsic CNT properties are also affected due to the breakage and π-disruption [16].

Sidewall cycloadditions (e.g. 1,3 dipolar and [4+2] Diels-Alder) have emerged as a promising alternative to acidic oxidations in biomedical applications, due to the superior balance between preservation of intrinsic properties and maximization of CNT biodegradability [12, 17, 18]. Cycloaddition reactions to CNTs involve the covalent bonding of cycloadducts to two adjacent sp^2 C atoms of the CNT hexagonal lattice. In these bonding, the cycloadduct disrupts the sp^2 C-C structure into sp^3 geometry at two neighboring C atoms, weakening but not breaking the C lattice. Cycloaddition reactions of 1,3 dipolar groups were ascribed to the longitudinal unzipping of CNTs, observed under ultra-high vacuum scanning tunneling microscopy conditions, as described by Paiva et al. [19]. Soon after, Bianco's group found other external stimuli that were able to cut or degrade 1,3 dipolar functionalized CNTs, in an *in vivo* harsh oxidative milieu [20].

Overall, cycloadditon reactions become promising functionalization strategies to tune the biocompatibility and biodegradability of CNTs. This gives a new perspective

on translation of CNTs into the clinic. While 1,3 dipolar cycloadditons have been widely studied following the pioneering work of Bianco's group for bioapplications [21], the [4+2] Diels-Alder cycloaddition route has received less attention since its first attempt by Delgado et al. [22]. Yet, both show similar potential to functionalize CNTs [23] and to render them biocompatible and biodegradable.

A Diels-Alder based functionalization with potential for biomedical purposes was proposed by Proença et al. [23]. The covalent functionalization starts by bonding the "anchor" group (hydrophobic group) resulting from the [4+2] Diels-Alder cycloaddition of 1,3 butadiene, followed by a soft oxidation of the alkene group with $KMnO_4$, to generate carboxylic groups (hydrophilic group). Each group has specific functionalities. The hydrophobic group controls the colloidal stability (steric stabilization) and biodegradation, altogether with minor damage to the CNT intrinsic properties; and the hydrophilic group promotes the colloidal stability (electrostatic stabilization), the bonding of active biomolecules (e.g. proteins, carbohydrates, nucleic acids) and gives negative electrical charge CNT surfaces. The latter functionalities granted by the carboxylic groups also govern the CNT interfacing with bone tissue [24]. Regarding the surface polarity, those negatively charged have shown superior *in vitro* and *in vivo* performances in osteoblastic cells adhesion/proliferation and acceleration of bone bonding than positively charged ones [25].

The present work focuses on the *in vitro* and *in vivo* evaluation of the toxicological profile of multi-walled carbon nanotubes (MWCNTs) membranes functionalized by the [4+2] Diels-Alder cicloaddition reaction of 1,3 butadiene. The CNT membranes were fully characterized considering the functionalization yield, functional groups recognition, surface charge, wettability and roughness. Due to the relevance and promising applications of Diels-Alder functionalized CNTs in bone tissue-related applications, *in vitro* testing was conducted with human osteoblast-like cells to assess their viability/proliferation. The *in vivo* experiments of subcutaneous implantation of CNTs in rats aimed to address their biocompatibility and biodegradation.

Materials and Methods

Production, purification and functionalization of CNTs

Vertically aligned CNTs (VACNTs) were synthesised by an optimised catalyst-supported chemical vapour deposition (CVD) technique [9], as sketched in Fig. 1a. Prior to the synthesis step, the 2 inch diameter p-type Si/SiO_2 wafer (Siegert Consulting) substrates for the CNT growth were coated with a bilayer of Al_2O_3 (10 nm)/Fe (1 nm), by magnetron sputtering. Then, the Fe film was converted into nano-sized particles (~20 nm) with a round shape morphology and a uniform density (~10^{10} particles.m^{-2}) by means of an *in situ* annealing, inside the CVD reactor, at 770ºC, under a reductive gas flow of H_2/Ar (500/200 sccm) (Fig. 1a). Subsequently, the H_2 and Ar flows were adjusted to 400 and 100 sccm respectively, and the C_2H_2 flow (10 sccm) was added for 15 min to yield the Fe-catalysed growth of VACNTs with diameter and length sizes of ~15 nm and ~1.5 mm, respectively, on large areas (Figs. 1a to 1c). These pristine CNTs are almost free of metal impurities with a purity level of >99.9 wt.%, assessed by ICP-AES[9]. Large VACNTs blocks were then removed from the Si substrate using a polymeric spatula and then dispersed in ethanol/water (3:1) suspensions. Subsequent mechanical mixing steps of high-speed shearing (IKA T25-Ultra-Turrax, working at 20500 rpm) and sonication (Selecta, working at 60 kHz, 200 W) steps for 15 min and 60 min, respectively, were applied to disentangle the bundles of tubes. Ultimately, the suspension of CNTs was freeze-dried (Labconco, LYPH Lock 4.5, Kansas City, MO), at -30ºC under vacuum for 96h, to obtain a final fluffy CNT powder with minimal agglomeration and maximum specific surface area, designated here as CNTs (Figs. 1d

and 1e). Both features are favorable to improve the yield of the subsequent purification and functionalization processes.

CNT purification was performed in an open graphite crucible inside a graphite furnace, at 1900 ºC for 8 h. This process was done under highly pure Ar (purity> 99.9999%) atmosphere a fixed flow of 20 sccm to drag-out vaporized impurities.

CNTs were functionalised using a two-step functionalization method [23] based on the Diels-Alder cycloaddition reaction of 1,3-butadiene (Bu), forming cyclohexene at the CNTs surface followed by oxidation of the alkene formed under mild conditions to form carboxylic acid groups (COOH) (Fig. 2a). Approximately 70 mg of CNTs were suspended in a solution of equal weight of sulfolene (≥98%, Sigma-Aldrich) in 20 ml of diglyme (≥99.5%, Sigma-Aldrich), in a round-bottom flask. The suspension was heated to 150 ºC to induce the slow decomposition of sulfolene, generating sulphur dioxide and Bu. The end of the sulfolene decomposition was detected when a filter paper soaked with an aqueous solution of potassium dichromate, placed at the top of the condenser, no longer changed the colour from orange to blue/green. The reaction proceeded for 24 hours, the CNTs were collected by filtration using a 0.22 μm pore size polycarbonate membrane (Millipore) and carefully cleaned to eliminate the solvent. This process was done by sonication in ethanol (≥99.9%, Sigma-Aldrich) for 5 min followed by washing with ethyl ether (≥98%, Sigma-Aldrich). The solid was then vacuum dried at 100ºC for 48 h. The alkene functional groups of the Diels-Alder functionalized CNTs were further converted into carboxylic acid groups (COOH) by oxidation with a 0.1 M aqueous solution of KMnO4 (≥99%, Sigma-Aldrich), stirring for 30 min at room temperature. After oxidation, the CNTs were filtered, washed with distilled water and dried at 100ºC in the vacuum oven for 5h. A blank test performed by treating the pristine CNT with 0.1 M KMnO4 solution under similar conditions (stirring for 30 minutes under ambient conditions) confirmed the absence of reaction (no increase in weight loss was detected by TGA).

Preparation of CNT membranes

CNTs were re-suspended in isopropyl alcohol (≥99.8%, Sigma-Aldrich) with a concentration of 0.1 $g.l^{-1}$ by the two-step mechanical mixing method described in section 2.2. Afterwards, the CNT suspension was dropped in a cylindrical mould of 10 mm of diameter placed on a 0.22 µm pore size disc filter (hydrophobic PTFE, Millipore), to produce CNT membranes by vacuum filtration. This was accomplished by a rotary vacuum pump connected to the filter-Büchner funnel-Kitasato flask setting. For each CNT membrane of 10 mm of diameter (Figs. 1f and 1g), about 4 ml of suspension was used. After filtration, the membranes were dried in an oven at 80ºC for 15 min. The membranes were sterilized by UV radiation for 12 h prior to the biological testing.

Characterization of CNT membranes

CNT impurities of amorphous carbon and inorganic types were quantified by thermogravimetry (Setsys Setaram) in N_2 (TG_{N2}) and O_2 (TG_{O2}) atmospheres, respectively. The samples were heated at 10 ºC/min under a constant gas flow of 200 sccm. Quantitative measurements of the chemical fuctionalization were performed by BET analyses (Micromeritics Gemini 2370 V5). For accurate measurements, the samples were firstly dried in an oven for 24h at 80ºC. Eight partial pressures were applied to further calculate the surface area after degassing the samples in N_2 at 120ºC for at least 2 h. The acid-base characterization of the CNTs was carried out by base titration under similar conditions to those described by Gorgulho et al. [26]. Approximately 100 mg of CNTs were suspended in a HCl solution (0.01 M) so that all the titrations started at a pH ~ 2. The suspension was stirred under inert atmosphere (Ar) during 15 min. The potentiometric titration started with the addition of 2 mL of a 0.1 M NaOH (aq)

solution, continuing with the addition of 0.01 mL/min aliquots until reaching pH = 11. The electrode was protected with a dialysis membrane, previously neutralized. Infrared spectroscopy (FTIR, Bruker, IFS 55) was applied to inspect the chemical groups on the sidewalls of the CNTs. The spectra were collected by a golden gate attenuated total reflectance (ATR) configuration using a diamond tip with a resolution of 4 cm^{-1} in the wavenumber range of 400-4000 cm^{-1}. Quantitative and qualitative examinations of the organic chemical groups were also accomplished by X-ray photoelectron spectroscopy (XPS, VG Scientific ESCALAB 200A). The spectra were acquired using a non-monochromatized AlKα radiation (1486.6 eV, 300 W) working at 15 keV, with a step size of 0.10 eV and a dwell time of 1s. The polarity and density of electrical charges of the CNTs were estimated zeta potential (ZP) analyses in a Zeta-meter equipment (Malvern, Zetasizer Nano Series) in an electrolyte aqueous solution of 0.01M of KCl. The experiments were performed in quintuplicate at pH:7, adjusted with 0.001 M HCl and 0.001 M NaOH solutions, and the ZP was calculated according to Smoluchowski's equation [27].

DC electrical conductivity measurements of CNTs were accomplished to investigate on the level of π-disruption promoted by the chemical fuctionalization. Disc-shaped CNT membranes of 10 mm in diameter and 14±3 μm thick were prepared by vacuum filtration. Following a Van der Pauw configuration, for of each sample, four copper wires were fixed with a high conductive silver glue (RS, $\sigma > 1\times10^{5}$ $\Omega.m^{-1}$) to two pairs of diametrically opposite contact positions. While the current was passing between one pair of contacts the voltage was measured along the other pair, perpendicular to the first pair. The I-V data was acquired by a computer-controlled 16-bit high-speed board (National Instruments DAQPad-6015) with a stepped applied voltage of 0.5 V in the range of -10V to 10V at 1s time intervals at room temperature.

High resolution scanning microscopy (HR-SEM, Hitachi SU70 working at 15 keV with a resolution of 1 nm) was used to analyse the microstructure of the CNT membranes. The purity of the samples was assessed by energy dispersive

spectroscopy (EDS, Bruker Quantax 400). Scanning transmission electron microscopy (STEM), performed with a transmitted electron detector coupled to the HR-SEM equipment, was applied to observe the global position of the organic deposits of the CNTs. For more detailed examination of the CNT sidewalls, a high-resolution transmission electron microscopic (HR-TEM, JEOL 2200FS working at 200 keV, resolution of 0.1 nm) was accomplished. STEM and HRTEM samples were prepared by suspending CNTs in isopropyl alcohol (≥99.8%, Sigma-Aldrich) and dropping the suspension on lacey-carbon Cu grids (Agar Scientific), and drying afterwards in a vacuum oven at 100ºC for 30 h to reduce contamination.

The structural insights of as-prepared and *in vivo* implanted CNT membranes were inspected by *μ*-Raman spectroscopy. For that, a Jobin Yvon HR800 (Horiba, Japan) micro-Raman apparatus was used in the backscattering configuration. The selected 532 nm laser line was provided by a Nd:YAG DPSS laser (Ventus, Laser Quantum, UK). The spectra were acquired using a 1800 l/mm grating, while the Rayleigh rejection was accomplished by edge filtering allowing Raman acquisition from 50cm-1. In order to optimize the collection conditions, a 100x objective (spot size ~1μm, NA=0.85, Olympus, Japan) was used, focusing the laser excitation onto the sample and collecting the backscattered Raman radiation into the spectrometer to be further detected by a Peltier cooled (223K) CCD sensor. The spectrometer was operated in the confocal mode, setting the iris to 300μm, while the acquisition time was set to 45 seconds with 5 accumulations. The laser power was monitored in order to avoid any damage by local overheating, always keeping the radiation level below 0.2mW/μm2. Each spectrum was averaged from the data collected at three randomly selected spots. The in-plane crystallite size (L_a) of CNTs was estimated by measuring the ratio of the integral area of the D-band and G-band (Cançado's equation [28]).

A sessile drop technique assisted by a video-based software interface (DataPhysics OCA 20) was used to measure the contact angle of the CNT membranes. For this, the CNT membranes were previously fixed on a glass slice and

clean three times with distilled and deionized water, followed by overnight drying in an oven at 80ºC. For a typical contact angle measurement, a drop of 1 ml of distilled and deionized water was gently dropped on the surface of the membrane using a micrometric syringe. At this point, the drop starts to be recorded over time by a CCD-camera. A single video frame was then selected to calculate the contact angle. This frame corresponds to the instant of the water drop stabilization just after the contact with the surface of the membrane. A Laplace-Young mathematical function, suitable for the measurement of high contact angles, was used to fit the contour line of the drop. No less than 5 drops were analysed.

The average surface roughness (S_a) parameter of the membranes was determinated using a profilometer (Sensofar S-Neox, with a 100X lens). The equipment was operated under topographic imaging, in confocal mode, using white light (to improve signal from the dark samples). The images were acquired, without averaging, using the equipment minimum of 0.2 micrometer per vertical step, for a total of about 150 sections acquired per image. For each acquisition, at least 95% of the image was built using original data. MountainsMap software from DigitalSurf was used to further process the data acquired. Each original image was levelled to remove unwanted inclination, extraneous data points were removed and the non existing data points were filled using an averaging filter from neighbouring data. A Gaussian filter of 25 μm was then used to remove the long range surface roughness of the somewhat wrinkled surfaces, and both resulting topographic images, the filtered data and the removed topographic data, were analysed using software routines to yield roughness data according to standard ISO 25178 and to produce representative linear roughness profiles. The peak count parameter (R_{pc}) was assessed using a linear profilometer (Perthometer Mahr M1) by averaging 5 acquisitions per sample.

Evaluation of the biological behavior – in vitro testing

Human osteoblast-like cells (MG63 cells, ATCC number CRL-1427™) were cultured in α-Minimal Essential Medium (α-MEM), supplemented with 10% fetal bovine serum, 50 $\mu g.ml^{-1}$ ascorbic acid, 50 $\mu g.ml^{-1}$ gentamicin and 2.5 $\mu g.ml^{-1}$ fungizone, at 37ºC, in a humidified atmosphere of 5% CO_2 in air. For sub-culturing, the cell layer (at around 70-80% confluence) was detached with trypsin – EDTA solution (0.05% trypsin, 0.25% EDTA), for 5 minutes, at 37ºC and a single cell suspension was prepared in complete supplemented culture medium. Cells were cultured ($5x10^4$ $cells.cm^{-2}$) on the surface of *p*-CNTs and *p,f*-CNTs membranes, for 4 days. Colonized membranes were evaluated for cell adhesion and morphology by confocal laser scanning microscopy (CLSM) and scanning electron microscopy (SEM) and for cell viability/proliferation (3-(4,5-Dimethylthiazol-2-yl)-2,5-diphenyltetrazolium (MTT) and lactate dehydrogenase (LDH) assays) and alkaline phosphatise (ALP) activity. Cells cultured on standard tissue culture plates were used as control.

For CLSM observations the cells grown over the samples were fixed (3.7% methanol-free formaldehyde, 15 minutes), permeabilized with 0.1% Triton, and incubated with bovine serum albumin (Sigma Aldrich), 10 $mg.ml^{-1}$ in PBS, for 1 hour, in order to block non-specific interactions. Cytoskeleton filamentous actin (F-actin) was visualized by treating permeabilized cells with Alexa Fluor® 488-conjugated phalloidin (Invitrogen), 1:100 in PBS, for 20 minutes. Cells were counterstained with propidium iodide (Sigma Aldrich), 10 $mg.ml^{-1}$ in PBS, for 5 minutes. Stained samples were mounted in Vectashield® (Vector laboratories) and examined in a Leica SP5 AOBS (Leica Microsystems®) microscope. To perform the SEM observation of the samples they were fixed (1.5% glutaraldehyde in 0.14M sodium cacodylate buffer, pH 7.3, 10 minutes), and dehydrated in graded alcohols and critical-point dried. Previously to SEM

observation, samples were sputter-coated with gold and analyzed in a FEI Quanta 400FEG ESEM.

The MTT assay is based in the ability of mitochondrial dehydrogenase to reduce the MTT to a dark blue formazan product. MTT (0.5 $mg.ml^{-1}$) was added to each well, and the cultures were incubated for 3 hours at 37ºC. Following, the formazan salts were dissolved in dimethylsulphoxide (DMSO) and the absorbance (A) was determined at λ = 600 nm on an Elisa reader (Synergy HT, Biotek). The LDH assay is based on the reduction of NAD by the action of LDH released to the medium. The resulting reduced NAD (NADH) is utilized in the stoichiometric conversion of a tetrazolium dye. Determination of the total LDH was performed in the cultures using the *In vitro* toxicology assay kit lactate dehydrogenase based (Sigma-Aldrich; St. Louis, MO), according to the manufacturers' instructions. The amount of LDH leakage to the medium was normalized by total LDH, and calculated as follows: LDH leakage % = LDH medium / total LDH x 100. ALP activity was evaluated in cell lysates (0.1% Triton X-100, 5 min) by the hydrolysis of *p*-nitrophenyl phosphate in alkaline buffer solution (pH~10.3; 30 min, 37 ºC) and colorimetric determination of the product (*p*-nitrophenol) at 400 nm in an ELISA plate reader (Synergy HT, Biotek). ALP activity was normalized to total protein content (quantified by Bradford's method) and expressed as $nmol/min.mg_{protein}^{-1}$.

For improving data quality, three independent experiments were performed; in each experiment, three replicas were accomplished for the biochemical assays and two replicas for the qualitative assays. Results are presented as mean ± standard deviation (SD). Groups of data were evaluated using a two-way analysis of variance (ANOVA) and no significant differences in the pattern of the cell behaviour were found. Statistical differences between experimental groups were assessed by Bonferroni's method. Values of $p \leq 0.05$ were considered statistically significant.

Evaluation of the biological behavior – in vivo testing

The study was performed in accordance with the authorization of the Local Ethical Committee and observed the technical standards of protection of experimental animals, according to the Portuguese (Decree No. 1005/92) and European (Directive 2010/63) legislations. Sixteen male Wistar rats, 95 – 105 days old (Harlan Laboratories, Germany) were used for subcutaneous implantation of prepared *p*-CNTs and *p,f*-CNTs membranes. Animals were housed in groups of 2 in type II cages, with water and food given ad libitum. Four implantation periods were evaluated: 3, 7, 21 and 49 days. General anesthesia was induced with the intraperitoneal (IP) injection of xylazine (10mg/kg) and ketamine (90mg/kg). The rats were monitored to ensure that an appropriate surgical plane of anesthesia was maintained throughout surgical manipulation. An IP injection of tramadol (10mg/Kg) was given for post-operative analgesia. The skin around the dorsum midline was shaved and disinfected with povidone-iodine solution and each animal was placed in a ventral position. Four small longitudinal incisions (~2 cm) were made on the dorsum, close to the midline, and a subcutaneous pocket was bluntly dissected at each incision with blunt tweezers. A single membrane was placed in each pocket. A total of eight membranes per experimental group, per time point, were implanted (four rats per time point). Following, each incision was closed with simple interrupted absorbable 4/0 sutures (Vicryl Rapide® - polyglatin 910, Ethicon, Livingston, UK). Each animal received a subcutaneous injection of tramadol (10 $mg.Kg^{-1}$) at 12, 24 and 36h after surgery for continued post-operative analgesia. Animals were monitored daily for any complications or abnormal behaviour. After euthanasia, segments of the subcutaneous tissue including the areas of the implanted samples were retrieved and excised and processed for histological observation. Harvested specimens were fixed in 10% neutral

buffered formalin. Tissues were embedded in paraffin and thin sections were cut and stained with haematoxylin and eosin to evaluate the tissue response to implanted *p*-CNTs and *p,f*-CNTs. Specimens were characterized by optic microscopy. To accomplish the peroxidase histochemistry all samples collected 48 hours after implantation were immediately frozen on -20ºC and cut in the horizontal plane on a cryostat (HM520 Microm) into 5-µm sections. Peroxidase activity was demonstrated using DAB (*3,3'-diaminobenzidine)* (Merck®) as the enzyme substrate. The incubating medium consisted in one DAB buffer tablet dissolved in 10 ml distilled water (pH 6.85) and 40 µl of 3% H_20_2. The sections were incubated with DAB (pre-heated to 37ºC) for 10 minutes, then washed thoroughly in distilled water, counterstained with hematoxylin, dehydrated and mounted with Entellan (Merck®) for evaluation by light microscopy.

Results and Discussion

Diels-Alder functionalized CNT membranes characterization

As stated in the introduction, Diels-Alder functionalized CNTs were designed with chemical groups to maximize their biodegradability and biocompatibility. CNTs were functionalized starting by a Diels-Alder reaction to form a chain of 1,3-butadiene cycloadducts (hydrophobic groups, highlighted in green in the sketch of Fig. 2a) following by an oxidation of the end alkene groups to produce carboxylic groups (hydrophilic groups, highlighted in red in the sketch of Fig. 2a).

Covalently bonded chains of cycloadducts with highly dense arrangement on the CNT outer sidewalls are designated here as an organic coating. To evaluate the uniformity and thickness of this coating, STEM and HRTEM analyses were performed (Figs. 2b-e). The low magnification STEM images of Figs. 2b and 2c clearly shows uniformly coated *p,f*-CNTs at long-range and clean p-CNT, both free of metallic

impurities. Further details on the CNT sidewalls are given by high resolution TEM images (Figs. 2d and 2e). Fig. 2d shows clean walls free of metallic nanoparticles and amorphous carbon. On the other hand, Fig. 2e confirms the uniformity of a ~2 nm thick organic coating on the *p,f*-CNT sidewalls.

The TEM images also shown both CNT types with high structural organization presenting carbon walls perfectly aligned with the tube's axis (Figs. 2d and 2e). The in-plane crystallite size (L_a), listed in Table 1, corroborates these observations, showing no significant change of structural crystallinity with the organic coating. The L_a values are inversely proportional to the ratio of the integrated areas of the D-band and G-band (ID/IG), according to Cançado's equation [28]. The ID/IG was observed to be lower for *p,f*-CNT compared to *p*-CNT (EIS, Fig. 1S). This decrease of the D-band area for the CNTs with an organic surface coating may be related to a damping effect, reducing the in-plane vibrations assigned to this band. The same effect was observed before for commercial CNTs (Nanocyl, NC7000) functionalized by the two-step procedure described here, under the same reaction conditions (EIS, Fig. 2S). The functionalized NC7000 were also characterized by a lower ID/IG ratio compared to purified NC7000. After heating the former to 1000 ºC under N_2 (g) the resulting nanotubes, clean from the organic functionalization, recovered the Raman signature of the purified NC7000, showing that the original nanotube structure remained unchanged (EIS, Fig. 2S). Thus, the CNTs functionalized by the Diels-Alder cycloaddition reaction did not show evidence for structural damage, contrarily to the observations reported for CNTs functionalized with strong oxidizing acids (EIS, Fig. 1S).

To further demonstrate this, TG_{O2} and TG_{N2} curves were performed (EIS, Fig. 3S). For p-CNT and p,f-CNT samples, the TG_{O2} curves at 1200 ºC indicate that both samples were completely burned, i.e. non-measurable ash residues were depicted, which is suggestive of the absence of inorganic impurities. The EDS results (EIS, Fig. 4S) also prove the absence of contaminants, only a negligible trace of S element was detected in the p,f-CNT sample derived from the sulfolene used as regent in the

functionalisation process. Also, the oxidation temperatures (TG_{O2}) of p-CNT and p,f-CNT samples are close, of 681ºC and 695ºC, proving the preservation of the CNT structure when submitted to the functionalization process (EIS, Fig. 3S). Below the oxidation temperature, the *p,f*-CNTs suffer from partial weight losses due to gradual elimination of organic groups [23]. The respective TG_{N2} confirms the large grafting of an organic coating by yielding a weight loss of ~21% (EIS, Fig. 3S). The TG_{N2} curve of the *p*-CNTs reveals that the sample is almost free of amorphous carbon since no weight loss was detected up to 1000ºC (EIS, Fig. 3S). These results are in accordance with the STEM and TEM observations (Figs. 2b-e).

Surface area and electrical conductivity values presented in Table 1 also indicate the significant deposition yield of the organic coating on the CNT sidewalls by giving a reduction of ~40 % and ~70 % , respectively.

The acid-base characteristics of the functionalized materials indicate their acidic character (EIS, Fig. 5aS). The control and the aqueous suspension of *p*-CNTs reached a neutral pH:7 at a lower concentration of NaOH compared to *p,f*-CNTs, the former requiring ~ 3.6 ml and the latter ~ 4.2 ml of NaOH solution. The identification of these acidic groups was accomplished by FTIR (EIS, Fig. 5bS). The spectrum of the *p,f*-CNT sample reveals the presence of carboxylic (COOH) functional groups with typical signature peaks for carbonyl (C=O) at 1735 cm^{-1}, for hydroxyl (-OH) at 3449 cm^{-1} (H-bonded), at 1365 cm^{-1} for O-H bending, and at 1212 cm^{-1} for C-O stretching [29, 30]. The peak at 1040 cm^{-1} may be attributed to S=O stretching associated to sulfonic acid groups [31]. Adsorbed CO_2 molecules were also detected at 2340 cm^{-1} [32], but only on the reactive surface of the *p,f*-CNT samples. Both p-CNT and p,f-CNT samples present small peaks at 3012 and 1426 cm^{-1} that may be attributed to C-H stretching in aryl-H type of bonds and saturated C-H deformations, respectively.

Further evidence for the acidic nature of the functionalized CNTs was obtained by XPS. Fig.3a depicts the survey spectra showing the typical C1s and O1s peaks, the latter clearly more intense for the *p,f*-CNT, corresponding to twice the O:C ratio relative

to *p*-CNT (Table 2). This observation is consistent with the FTIR analyses presented previously. The shape of the high-resolution C1s spectra is characterized by a main component peak corresponding to the sp2 carbon of the graphite-like lattice and a strong tailing toward higher binding energy (Fig. 3b).

Four additional peaks were necessary to obtain a good fit, that may be assigned to C-O (~286 eV), >C=O (~287.5 eV), -COO (~288.5 eV), and the higher energy shakeup peaks due to $\pi \rightarrow \pi^*$ electron transitions. The peaks resulting from curve deconvolution are present in both types of CNT, showing higher intensity for the *p,f*-CNT relative to *p*-CNT. The detailed information of the peak areas obtained by deconvoluting the C1s and O1s peaks is presented in Table 2.

The high resolution O1s spectrum obtained for *p*-CNTs could be deconvoluted into two main component peaks centred at approximately 532 and 533.8 eV, typically corresponding to O-C=O and O-C=O, respectively. These component peaks are still present in the O1s deconvolution for *p,f*-CNTs (slightly shifted) and an additional intense peak centred at 533 eV, that may be assigned to C-OH [30]. Inspection of Table 2 confirms that *p,f*-CNT samples have higher concentration of carboxylic groups (peaks P4 and P3') than the *p*-CNT samples. These XPS observations corroborate with the FTIR analysis. Furthermore, considering the O/C atomic ratio measured by XPS, correcting for the oxygen present before the Diels-Alder reaction, the functionalization degree of p,f-CNT is estimated as roughly one functional group per forty carbon atoms of the CNT surface. This estimate was obtained considering that the major oxidation product is carboxylic acid.

Surfaces supplied with -OH or -COOH groups are expected to be both negatively charged (δ-) due to their high tendency to ionize by losing the H^+ ion [33]. Also, it can be assured that *p,f*-CNTs have higher density of electrical charge than the *p*-CNTs due to the higher level of the referred groups, according to the data already shown. Zeta potential and wettability measurements were carried out to verify the chemical analysis results obtained. Table 1 confirms that *p,f*-CNTs samples exhibit

higher negative potentials than purified ones, -50 and -34 mV, respectively. Similar observations were previously observed in isopropyl alcohol [34]. Moreover, the wettabilitty measurements are in accordance with the zeta potential values by showing *p,f*-CNTs samples with an average contact angle of 123º, lower than 135º of the *p*-CNTs.

Topographical features of Diels-Alder functionalized CNT membranes

Fig. 4 depicts representative SEM micrographs of the p-CNTs and p,f-CNTs membranes. Overall, they have rough surfaces (Table 1) resulted from the arrangement of rough areas of micrometer-sized positive and negative protrusions interspaced by smooth areas of horizontally disposed nano-rough tubes (Figs. 4a-c). The nano-scale roughness of CNT membranes is in a well-known range values that depends on the outer diameter of entangled individual CNTs that form the membrane[35, 36]. MWCNTs membranes produced with 10-30 nm thick tubes, a diameter range similar to that of our CVD grown CNTs (Fig. 4c), have typical nanoroughness values between 40 and 60 nm [36] Additionally, distinct topographic features are seen between the two membrane types (Figs. 4a and 4b). Particularly, the p,f-CNTs membrane presents higher linear frequency of local positive protrusions, given by the peak count parameter R_{pc} (Table 1), and lower surface roughness Sa, which indicates a more homogeneous surface topography. Colour surface height maps showing in detail the differences between samples and the respective linear roughness profiles are presented in Fig. 6S (see EIS).

***In vitro* human osteoblastic cell response on Diels-Alder functionalized CNT membranes**

Adhesion of MG-63 osteoblastic cells to the standard tissue culture plates (control cultures) and to *p*-CNT and *p,f*-CNT membranes was evident soon after plating, as seen on the CLSM images taken at day 1 (Fig. 5a). However, evident differences were observed in the cytoplasmic expansion. Cell spreading was clearly improved on the functionalized membranes, where a significant percentage of cells exhibited an elongated morphology, similarly to that on control cultures, contrasting to the rounded appearance of most cells on *p*-CNT (Fig. 5a). Differences on the cell morphology and cell interaction with the membrane surface subsist throughout the culture time. Cultures growing on *p*-CNT appeared as clusters of rounded cells, unable to individualize, evidencing difficulties in expanding the cytoplasmic onto the membrane surface (Fig. 5a). By contrast, on *p,f*-CNT, well-spread cells were able to adapt to the irregular surface topography and to establish intimate cell-to-cell and cell-to-membrane interactions via cytoplasmic expansion (Fig. 5a). This behavior is similar to that observed in standard tissue culture plates (Fig. 5a).

Results for cell compatibility tests are given in Fig. 5b. Cell viability/proliferation, assessed by the MTT assay, increased throughout the culture time in control cultures and on both membranes. At day 1, values were similar on the three substrates, suggesting similar numbers of attached/viable cells. For longer culture times, MTT reduction values were higher on *p,f*-CNT compared to p-CNT, supporting an enhanced cell viability and/or growth rate on the functionalized samples. This behaviour was similar to control cultures, although values were slightly lower on *p,f*-CNT (about 20%). Regardless, no significant differences were found between cultures grown on control and *p,f*-CNT. The LDH released to the medium was higher on *p*-CNT membrane, evidencing signs of cellular toxicity, namely membrane integrity, which might explain the lower MTT reduction values compared to those on control and on *p,f*-CNT samples. Cells synthesized ALP, an early osteoblastic marker. Enzyme activity was low on *p*-CNT samples but high, and similar to control, on *p,f*-CNT membranes. Overall, the results suggest that the functionalized membranes allowed a slightly lower proliferation

rate but a similar functional activity of the osteoblastic cells compared to the standard tissue culture plates. Additionally, the membrane integrity was maintained in both *p*-CNT and *p,f*-CNT throughout the culture time, as shown by high magnification SEM images (EIS, Fig. 7S).

Literature reports addressing the cytocompatibility of CNTs-containing materials reveal divergent results, ranging from a dose-dependent impairment of the cellular metabolic activity/proliferation, to the absence of cytotoxicity, and even to the enhancement of cellular function, as recently reviewed [37]. Regarding the response to osteoblastic cells, a general trend for a biocompatible profile is verified. Appropriate cellular adhesion and early proliferation has been reported in studies involving several osteoblastic cell systems, i.e. in SaOS2 cells seeded over SWCNTs films prepared by different techniques and reporting different degrees of purity [38], MWCNTs sheets [39], and compact MWCNTs constructs [40], in rat osteoblast-like cells (MC3T3-E1 cell line) cultured over MWCNTs-covered culture plates [41], and human mesenchymal stem cells (hMSCs) cultured on a thin layer of SWCNTs [42] or monolayer patterns of CNTs [43]. Concerning the functional activity, increased alkaline phosphatase activity, osteoblastic gene expression and calcium deposition were seen in SaOS2 grown over compact MWCNTs [40] or CNTs grown from anodized titanium alloys [44], and the interaction of hMSCs with MWCNTs substrates lead to an induction of the expression of osteogenic markers [45].

On the whole, literature data strongly suggest that two key parameters, surface roughness and surface energy density, have rendered the modulation of the *in vitro* biocompatible profile of CNTs interfacing osteoblastic cells. Suitable cell adhesion and early proliferation observed over CNTs surfaces might be, at least, in part related to the nanoscale roughness profile. It has been shown that such nanoscale features are able to tune osteogenesis by a cell membrane distortion mechanism [46]. As suggested recently, the increased tension over actin filaments, derived from the bloated cytosolic expansion, may determine cellular events that converge to an enhanced osteogenesis

via the activation of Rho-family GTPase signaling [46]. Beyond the distortion-induced phenomenon, CNT surfaces are also able to interfere with biomolecules distribution, including that of talin, α-actinin, filamin and vinculin [47]. These focal adhesion proteins greatly determine early and late adhesion events and seem to temper the subsequent cell proliferation process [48]. Related to this, increased expression of focal adhesion proteins was reported on CNTs substrates [49].

The surface roughness parameters evaluated for the membranes (Table 1) are not sensitive to nanoscale features. However, the R_{pc} value for the *p,f*-CNT (9 peaks.mm^{-1}) portraits more anchorage sites to cells, with dimensions in the range 20-50 μm (Fig. 5a), than the corresponding value for the *p*-CNTs. Thus, the topography of the former (Fig. 4b) turn them friendlier for cell adhesion and proliferation [50]. In addition, the modifications introduced within the CNTs surface energy by functionalization may determine the success of the early adhesion and cell proliferation/differentiation events. For example, hMSCs grown over oxygen-functionalized (negatively charged) SWCNTs monolayers showed improved morphology and enhanced osteogenic commitment, as compared to non-functionalized substrates [45]. Both the *p*-CNT and *p,f*-CNT are negatively charged, but they presented significant differences in the zeta potential values, which is expected to influence the composition, exchange events and stability of the protein layer that quickly forms on the reactive surface of the CNTs membranes, with a relevant role in the elicited cell response [51, 52].

Overall, CNTs substrates contribute for an appropriate proliferation and osteoblastic differentiation, yet, functionalized CNTs membranes evidenced clear improved cell response.

In vivo biocompatibility and biodegradability of Diels-Alder functionalized CNT membranes subcutaneously implanted in rats

The *in vivo* biological response to functionalized and non-functionalized membranes was evaluated following subcutaneous implantation in Wistar rats for 7, 21 and 49 days. At the necropsy, no macroscopic signs of significant inflammatory reaction or cellular exudate were found around the implanted membranes, for the assayed time points. Histopathological analysis revealed that both MWCNTs membranes triggered an inflammatory response, characterized by the presence of a chronic immuno-inflammatory infiltrate and associated encapsulated granulation tissue, broadly identified following 7 days post implantation. With increased implantation time, at 21 and 49 days, a denser inflammatory infiltrate was attained, despite that a slight milder response was verified with the implantation of non-functionalized MWCNTs (Fig. 6 and Table 3).

Nevertheless, the attained trifling inflammatory response for both MWCNTs membranes did not result in neutrophil infiltration, cell necrosis, or the presence of cell debris – processes associated with the development of an adverse biological response [53] – thus supporting the reduced cytotoxicity profile of the functionalized CNTs.

These results come in line with previously published reports addressing the *in vivo* biological response to pristine CNTs. Current insights tend to support the idea that highly pure and crystalline CNTs are broadly nontoxic and only activate a milder inflammatory response, as detailed in recent reviews [7]. Subcutaneous or intramuscular implantation of both SWCNTs and MWCNTs in rodents seems to induce a minor infiltration of inflammatory cells associated with CNTs encapsulation [54], as verified in this report. Still, biological output seems to be major dependent on the particularities of the CNTs physic-chemical profile [1].

The intraperitoneal or subcutaneous grafting of distinct size MWCNTs suspensions revealed a minor response for shorter and smaller CNTs, while the administration of longer fibers, induced a high grade and reactive inflammatory response [11]. Apart from CNTs size (i.e., diameter and length) their degree of purity also seems to be a determining factor affecting tissue response. The presence of impurities

in MWCNTs was found to induce the activation of a severe immune-inflammatory reaction – manifested by marked follicular dystrophy and alopecia - following subcutaneous implantation of sampled CNTs powder in mice or rats; while purified MWCNTs revealed minor cell infiltration and slight granulomatous reaction [55]. Our results regarding the subcutaneous implantation of a relative high dose (4 mg per animal) of highly pure and crystalline unfunctionalized MWCNTs in a membrane form are in line with published literature supporting the adequate biological response with only trifling inflammation and encapsulation, following 49 days of implantation.

The biological response to functionalized CNTs is far less scarce in the literature. Despite that most studies are focused on the response following systemic administration and little is known regarding local tissue implantation, published data seems to trail the idea that functionalization improves the biological profile of CNTs [56]. In our work, functionalized MWCNTs membranes implanted subcutaneously induced a slighter intense inflammatory response, in comparison to non-functionalized MWCNTs membranes. This distinct biological behaviour might be related to the fact that, while p-CNTs membranes kept their structure broadly unaltered throughout the 49 days of implantation, signs of membrane break up and loss of structural integrity with release of small CNTs fibrillary remnants, could be easily identified in *p,f*-CNTs membranes. This was verified right after the first 7 days of implantation and increased progressively with the implantation time (Fig. 6). At high magnification, implanted *p*-CNTs membranes seem to retain the structural integrity (Figs. 6e and 6g) while the *p,f*-CNTs membranes revealed an advanced cell-mediated degradation process (Figs. 6f and 6h). Small fibrillar remains of *p,f*-CNTs can be identified, dispersed throughout the inflammatory infiltrate area (Fig. 6f, labelled by red arrows), at the same time that phagocytes seem to uptake and digest the fibrilar debris, as evidenced by the intracellular accumulation of thinner *p,f*-CNTs fibrils (Fig. 6h, dotted red circle). A faster degradation of functionalized CNTs within the biological environment has been recently addressed in distinct literature reports outreaching their improved biosafety profile. Accordingly,

carboxylated and nitrogen doped MWCNTs were found to be hastily degraded by oxidative peroxidases and hydrogen peroxide, in a layer-by-layer exfoliation mechanism facilitated by side wall defects [57]. Furthermore, CNTs with carboxylated surfaces, unlike unmodified CNTs, underwent degradation in a simulated phagolysosomal assay, revealing both longitudinal splitting as well as oxidative degradation of the side walls [14]. *In vitro* assays with living cells also tend to support the biodegradation of functionalized CNTs in a process mediated by oxidative enzymes commonly found in phagocytic cells of the immune system. Human neutrophils were found to completely degrade functionalized carbon nanotubes following 12 hours of incubation, in a process mediated by myeloperoxidase (MPO) and NADPH oxidase [58]. Interestingly, functionalized-CNTs incubated with human macrophages were negligible degraded after 6 hours of incubation and following 12 hours, only around 13% of degradation was verified by infrared spectroscopy [58]. Attained results support the idea that peroxidase activity may be a determinant of the biodegradation of CNTs [12, 59], as macrophages contain far less levels of MPO than neutrophils [60], and thus are expected to induce a significantly slower biodegradation of functionalized CNTs.

In order to endorse the neutrophils-mediated activity in p,f-CNTs degradation, we evaluated the tissue response to CNTs membranes implanted for 72 hours, valuing the identification of peroxidases in tissue sections (EIS, Fig. 8S). Neutrophils recruitment and activation can only be disclosed during the acute phase response triggered by material implantation, usually lasting for a few days [60]. Following, the persistence of the implanted material leads to a chronic phase, largely characterized by the presence of differentiating monocytes, macrophages and lymphocytes [60, 61], as that attained in histopathological sections of the 7, 21 and 49 days implantation time. The 3 days time point was chosen in order to minimize the effect of the surgical trauma in short-term experiments, still enclosing the transition from the acute to the chronic phase response and thus, being able to disclose the effect of the early neutrophilic recruitment and activation [62, 63]. Attained tissue sections revealed a typical staining

corroborating peroxidase activity, generally dispersed throughout the immune-inflammatory infiltrate area, but particularly concentrated at the region neighbouring the implanted membranes (EIS, Figs. 8aS and 8bS). Qualitatively, the implantation of *p,f*-CNTs membranes induced a more intense peroxidase staining, as comparing to *p*-CNTs membranes implantation, corroborating the idea that neutrophilic peroxidases may assist on the individualization of functionalized CNTs and contribute to the degradation of the *p,f*-CNT membranes.

Figs. 7a and 7b show micro Raman spectra acquisition areas taken on subcutaneously implanted *p*-CNT and *p,f*-CNT membranes. In samples analyzed immediately after implantation (Figs. 7c and 7d), spectra are dominated by the standard main features in CNTs at ~1350cm^{-1} (D band), ~1580cm^{-1} (G band) and a right shoulder at ~1620cm^{-1} (D' band). While the G band is associated to the main C-C tangential E_{2g}vibration mode, D and D' are disorder induced double-resonance (DR) Raman bands. In fact, whereas the D band comes from the breathing modes of sp^2 rings, D' is due to an intravalley DR mechanism, both bands being activated by local defects [64]. Compared to the *p*-CNT, the *p,f*-CNT reveal a decrease in the D band intensity before contact with the biological medium (Figs. 7c and 7d). This mode originates on the presence of defects on sp^2 C rings. The functional groups attached to the C rings seem to have a damping effect on such vibrations, reducing the D band intensity (previously discussed in Section "Diels-Alder functionalized CNT membranes characterization"). This damping is also observed for the exposed *p*- and *p,f*-CNT, presenting a reduction of the D band intensity after 7 days of implantation (Figs. 7c and 7d). There is evidence for the presence of other species with characteristic Raman bands at 1380, 1505 and 1618cm^{-1} that may be adsorbed or covalently bonded to the MWCNT, both for *p*-CNT and *p,f*-CNT, with higher intensity for the latter. The functional groups on the *p,f*-CNT may react with the biological material, and that is evidenced by the persistent changes induced on the D and G modes after 49 days of exposure to the biological medium. After this long exposure period the *p*-CNT show an increase of the

D band intensity, indicating a partial recovery of their original structure, while the *p,f*-CNT present a nearly unchanged D band relative to the material exposed for 7 days.

After 49 days of implantation the Raman spectra of both types of nanotubes reveal a considerable intensity decrease for the frequencies associated to the bonded/adsorbed molecules, but this reduction is less pronounced for the *p,f*-CNT. In fact the *p,f*-CNT present a small increase of the G band intensity and width, and the bands at 1380 and 1505 cm^{-1}, observed under *in vivo* conditions, coalesce with the D and G bands, respectively. This may be an indication either that the biological molecules are stably bonded to the *p,f*-CNT surface or that a CNT structural amorphization might occur to some extension.

Functionalized MWCNTs were observed to disperse much better in biological milieus (Figs. 6a-d), therefore increasing the available surface for reaction or adsorption of other molecules. The increase in surface availability or opening of the membrane may be a direct consequence of the MWCNT chemical modification, or may be due to physical changes of the *p,f*-CNT under stress induced by *in vivo* biochemical conditions. Recent studies showed that the MWCNT functionalized by the Diels-Alder cycloaddition reaction used in the present work may unzip the outer MWCNT layer, forming functionalized graphene nanoribbons (*f*-GNR). This effect was observed in solution by the application of ultrasounds for a short period of time, and may be triggered under different types of stresses. It was observed under scanning tunneling microscopy conditions, for MWCNTs functionalized by another type of cycloaddition reaction, the 1,3 dipolar addition of azomethine yilides [19]. Also, it was recently proved that this functionalization boost the *in vivo* biodegradation of MWCNTs [20]. As so, there is strong evidence that cycloaddition reactions are able to tune CNT degradation by either longitudinal opening or simple cutting. If this biodegradation phenomenon is observed, the new formed semi-opened structures would be able to extend and flatten the surface available for interaction with biological environments depressing the intrinsic toxicological risks of the starting CNT needle-like materials.

Conclusions

The biocompatibility and biodegradability profiles of Diels-Alder functionalized CNT membranes were successfully studied by *in vitro* and *in vivo* assays.

In vitro suitable cell adhesion was observed onto *p*-CNT and *p,f*-CNT membranes due to the roughness profile. Yet, the surface energy was also determinant in the success of the early adhesion event. In line with this, cell spreading was clearly improved on the functionalized membranes. The enhanced cell spreading on *p,f*-CNT substrates also contributes for an appropriate proliferation and osteogenic differentiation, supported by higher MTT reduction values and ALP activity values in the *p,f*-CNT membranes than the *p*-CNT ones.

In vivo subcutaneously implanted CNT membranes in Wistar rats revealed that both materials triggered a chronic immuno-inflammatory infiltrate and associated encapsulated granulation tissue, but without neutrophil infiltration or cell necrosis. This supports the reduced cytotoxicity profile of the functionalized CNTs. Owed to their higher biological reactivity, *p,f*-CNT membranes induced a slighter intense inflammatory response relatively to *p*-CNT membranes. Also, signs of degradation and loss of structural integrity were identified in p,f-CNT membranes, but not in the p-CNT membranes. Further, it was identified that the faster *in vivo* biodegradation of p,f-CNT membranes might be related to the higher oxidative milieu, verified by the increased peroxidase activity, at early implantation time points.

In vitro and *in vivo* data suggest that CNTs display an adequate profile for biological interaction, especially in bone tissue related applications. Though, CNTs functionalization provides new opportunities to modulate the interaction between these materials and biological environments, holding a strong promise as novel systems for

drug delivery, or just systems with improved biocompatibility and biodegradability. Regarding the latter, observations put forward that cycloaddition reactions have a high balance between preservation of intrinsic properties and maximization of CNT *in vivo* biodegradability, thus presenting superior appetency to functionalize CNTs for biomedical purposes than conventional acidic functionalizations. Future work, including studies exploring other live tissues and a careful morphological evaluation of the CNT membranes, will be carried out to confirm this idea and to propose a biodegradation mechanism.

Acknowledgements

This work was developed in the scope of the project CICECO-Aveiro Institute of Materials (Ref. FCT UID /CTM /50011/2013), financed by national funds through the FCT/MEC and co-financed by FEDER under the PT2020 Partnership Agreement. The authors are very grateful to R.F. Araújo (Centre of Chemistry, Univ. of Minho) for the acid-base titration measurements, M. Ferro (Materials and Ceramic Eng. Dept., Univ. of Aveiro) for TEM observations, F.J. Oliveira (Materials and Ceramic Eng. Dept., Univ. of Aveiro) for the optical profilometry measurements and the assistance of Dr. Carlos Sá (Materials Centre, Univ. of Porto) for XPS analyses.

Electronic Supplementary Information (EIS)

Experimental details on the preparation of HNO_3 funcionalized CNTs and supplementary analyses (μ-Raman, TG, EDS, acid-base titration, FTIR, roughness measurements, SEM and optical images) are shown.

References

1. B. S. Harrison and A. Atala, *Biomaterials*, 2007, **28**, 344-353.
2. P. A. Tran, L. Zhang and T. J. Webster, *Adv. Drug Delivery Rev.*, 2009, **61**, 1097-1114.
3. M. Shimizu, Y. Kobayashi, T. Mizoguchi, H. Nakamura, I. Kawahara, N. Narita, Y. Usui, K. Aoki, K. Hara, H. Haniu, N. Ogihara, N. Ishigaki, K. Nakamura, H. Kato, M. Kawakubo, Y. Dohi, S. Taruta, Y. A. Kim, M. Endo, H. Ozawa, N. Udagawa, N. Takahashi and N. Saito, *Adv. Mater.* , 2012, **24**, 2176-2185.
4. H. Dumortier, S. Lacotte, G. Pastorin, R. Marega, W. Wu, D. Bonifazi, J.-P. Briand, M. Prato, S. Muller and A. Bianco, *Nano Lett.*, 2006, **6**, 1522-1528.
5. A. Shvedova, V. Castranova, E. Kisin, D. Schwegler-Berry, A. Murray, V. Gandelsman, A. Maynard and P. Baron, *J. Toxicol. Environ. Health, Part A*, 2003, **66**, 1909-1926.
6. H.-F. Cui, S. K. Vashist, K. Al-Rubeaan, J. H. T. Luong and F.-S. Sheu, *Chem. Res. Toxicol.*, 2010, **23**, 1131-1147.
7. I. C. P. Firme and P. R. Bandaru, *Nanomed. Nanotech. Biol. Med.*, 2010, **6**, 245-256.
8. K. Pulskamp, S. Diabaté and H. F. Krug, *Toxicol. Lett.*, 2007, **168**, 58-74.
9. D. Mata, R. Silva, A. Fernandes, F. Oliveira, P. Costa and R. Silva, *Carbon*, 2012, **50**, 3585-3606.
10. L. Lacerda, A. Soundararajan, R. Singh, G. Pastorin, K. T. Al-Jamal, J. Turton, P. Frederik, M. A. Herrero, S. Li, A. Bao, D. Emfietzoglou, S. Mather, W. T. Phillips, M. Prato, A. Bianco, B. Goins and K. Kostarelos, *Adv. Mater.* , 2008, **20**, 225-230.
11. C. A. Poland, R. Duffin, I. Kinloch, A. Maynard, W. A. Wallace, A. Seaton, V. Stone, S. Brown, W. MacNee and K. Donaldson, *Nat. Nanotechnol.*, 2008, **3**, 423-428.
12. A. Bianco, K. Kostarelos and M. Prato, *Chemical Chem. Commun.*, 2011, **47**, 10182-10188.
13. B. L. Allen, P. D. Kichambare, P. Gou, I. I. Vlasova, A. A. Kapralov, N. Konduru, V. E. Kagan and A. Star, *Nano Lett.*, 2008, **8**, 3899-3903.
14. X. Liu, R. H. Hurt and A. B. Kane, *Carbon*, 2010, **48**, 1961-1969.

15. K. J. Ziegler, Z. Gu, H. Peng, E. L. Flor, R. H. Hauge and R. E. Smalley, *J. Am. Chem. Soc.*, 2005, **127**, 1541-1547.
16. Y. J. Kim, T. S. Shin, H. D. Choi, J. H. Kwon, Y.-C. Chung and H. G. Yoon, *Carbon*, 2005, **43**, 23-30.
17. I. Kumar, S. Rana and J. W. Cho, *Chem. Eur. J.*, 2011, **17**, 11092-11101.
18. Y.-S. Lee and N. Marzari, *Phys. Rev. Lett.*, 2006, **97**, 116801.
19. M. C. Paiva, W. Xu, M. F. Proença, R. M. Novais, E. Lægsgaard and F. Besenbacher, *Nano Lett.*, 2010, **10**, 1764-1768.
20. A. Nunes, C. Bussy, L. Gherardini, M. Meneghetti, M. A. Herrero, A. Bianco, M. Prato, T. Pizzorusso, K. T. Al-Jamal and K. Kostarelos, *Nanomedicine*, 2012, **7**, 1485-1494.
21. A. Bianco, K. Kostarelos, C. D. Partidos and M. Prato, *Chem. Commun.*, 2005, 571-577.
22. J. L. Delgado, P. de la Cruz, F. Langa, A. Urbina, J. Casado and J. T. Lopez Navarrete, *Chemical Communications*, 2004, 1734-1735.
23. M. F. Proença, R. F. Araújo, M. C. Paiva and C. J. R. Silva, *J. Nanosci. Nanotechnol.*, 2009, **9**, 6234-6238.
24. M. M. Stevens, *Mater. Today*, 2008, **11**, 18-25.
25. T. Kobayashi, S. Nakamura and K. Yamashita, *J. Biomed. Mater. Res.*, 2001, **57**, 477-484.
26. H. F. Gorgulho, J. P. Mesquita, F. Gonçalves, M. F. R. Pereira and J. L. Figueiredo, *Carbon*, 2008, **46**, 1544-1555.
27. P. Hiemenz and R. Rajagopalan, *Principles of Colloid and Surface and Chemistry*, Marcel Dekker, New York, 1997.
28. L. G. Cancado, K. Takai, T. Enoki, M. Endo, Y. A. Kim, H. Mizusaki, A. Jorio, L. N. Coelho, R. Magalhaes-Paniago and M. A. Pimenta, *Appl. Phys. Lett.*, 2006, **88**, 163106-163103.
29. H. Peng, L. B. Alemany, J. L. Margrave and V. N. Khabashesku, *J. Am. Chem. Soc.*, 2003, **125**, 15174-15182.
30. J.-H. Zhou, Z.-J. Sui, J. Zhu, P. Li, D. Chen, Y.-C. Dai and W.-K. Yuan, *Carbon*, 2007, **45**, 785-796.
31. R. Xing, N. Liu, Y. Liu, H. Wu, Y. Jiang, L. Chen, M. He and P. Wu, *Adv. Funct. Mater.*, 2007, **17**, 2455-2461.
32. C. S. Chong, I. Ishak, R. H. Mahat and Y. M. Amin, *Radiat. Meas.*, 1997, **28**, 119-122.

33. H. Hu, A. Yu, E. Kim, B. Zhao, M. E. Itkis, E. Bekyarova and R. C. Haddon, *J. Phys. Chem. B*, 2005, **109**, 11520-11524.

34. D. Mata, F. J. Oliveira, M. Ferro, P. S. Gomes, M. H. Fernandes, M. A. Lopes and R. F. Silva, *J. Biomed. Nanotechnol.*, 2013, **10**, 725-743.

35. A. Martinelli, G. A. Carru, L. D'Ilario, F. Caprioli, M. Chiaretti, F. Crisante, I. Francolini and A. Piozzi, *ACS Appl. Mater. Interfaces*, 2013, **5**, 4340-4349.

36. F. Giubileo, A. Di Bartolomeo, M. Sarno, C. Altavilla, S. Santandrea, P. Ciambelli and A. M. Cucolo, *Carbon*, 2012, **50**, 163-169.

37. M. Uo, T. Akasaka, F. Watari, Y. Sato and K. Tohji, *Dent. Mater. J.*, 2011, **30**, 245-263.

38. M. Kalbacova, M. Kalbac, L. Dunsch and U. Hempel, *Carbon*, 2007, **45**, 2266-2272.

39. T. Akasaka, A. Yokoyama, M. Matsuoka, T. Hashimoto, S. Abe, M. Uo and F. Watari, *Bio-Med. Mater. Eng.*, 2009, **19**, 147-153.

40. L. Xiaoming, G. Hong, U. Motohiro, S. Yoshinori, A. Tsukasa, A. Shigeaki, F. Qingling, C. Fuzhai and W. Fumio, *Biomed. Mater.* , 2009, **4**, 015005.

41. M. Terada, S. Abe, T. Akasaka, M. Uo, Y. Kitagawa and F. Watari, *Dent. Mater. J.*, 2009, **28**, 82-88.

42. C. Y. Tay, H. Gu, W. S. Leong, H. Yu, H. Q. Li, B. C. Heng, H. Tantang, S. C. J. Loo, L. J. Li and L. P. Tan, *Carbon*, 2010, **48**, 1095-1104.

43. S. Y. Park, S. Namgung, B. Kim, J. Im, J. Y. Kim, K. Sun, K. B. Lee, J. M. Nam, Y. Park and S. Hong, *Adv. Mater.*, 2007, **19**, 2530-2534.

44. S. Sirinrath, Y. Chang, X. Xingcheng, W. S. Brian and J. W. Thomas, *Nanotechnology*, 2007, **18**, 365102.

45. K. Y. Baik, S. Y. Park, K. Heo, K.-B. Lee and S. Hong, *Small*, 2011, **7**, 741-745.

46. E. J. Arnsdorf, P. Tummala, R. Y. Kwon and C. R. Jacobs, *J. Cell Sci.*, 2009, **122**, 546-553.

47. J. Y. Lim, A. D. Dreiss, Z. Zhou, J. C. Hansen, C. A. Siedlecki, R. W. Hengstebeck, J. Cheng, N. Winograd and H. J. Donahue, *Biomaterials*, 2007, **28**, 1787-1797.

48. B. D. Cox, M. Natarajan, M. R. Stettner and C. L. Gladson, *J. Cell. Biochem.*, 2006, **99**, 35-52.

49. B. D. Holt, P. A. Short, A. D. Rape, Y.-l. Wang, M. F. Islam and K. N. Dahl, *ACS Nano*, 2010, **4**, 4872-4878.

50. C.-H. Choi, S. H. Hagvall, B. M. Wu, J. C. Y. Dunn, R. E. Beygui and C.-J. "Cj" Kim, *Biomaterials*, 2007, **28**, 1672-1679.
51. A. Verma and F. Stellacci, *Small*, 2010, **6**, 12-21.
52. I. Lynch and K. A. Dawson, *Nano Today*, 2008, **3**, 40-47.
53. J. M. Anderson, *Annu. Rev. Mater. Res.*, 2001, **31**, 81-110.
54. S. Koyama, M. Endo, Y.-A. Kim, T. Hayashi, T. Yanagisawa, K. Osaka, H. Koyama, H. Haniu and N. Kuroiwa, *Carbon*, 2006, **44**, 1079-1092.
55. S. Koyama, Y. A. Kim, T. Hayashi, K. Takeuchi, C. Fujii, N. Kuroiwa, H. Koyama, T. Tsukahara and M. Endo, *Carbon*, 2009, **47**, 1365-1372.
56. Z. Liu, W. Cai, L. He, N. Nakayama, K. Chen, X. Sun, X. Chen and H. Dai, *Nat. Nanotechnol.*, 2006, **2**, 47-52.
57. Y. Zhao, B. L. Allen and A. Star, *J. Phys. Chem. A*, 2011, **115**, 9536-9544.
58. V. E. Kagan, N. V. Konduru, W. Feng, B. L. Allen, J. Conroy, Y. Volkov, I. I. Vlasova, N. A. Belikova, N. Yanamala and A. Kapralov, *Nat. Nanotechnol.*, 2010, **5**, 354-359.
59. G. P. Kotchey, S. A. Hasan, A. A. Kapralov, S. H. Ha, K. Kim, A. A. Shvedova, V. E. Kagan and A. Star, *Acc. Chem. Res.*, 2012, **45**, 1770-1781.
60. S. Franz, S. Rammelt, D. Scharnweber and J. C. Simon, *Biomaterials*, 2011, **32**, 6692-6709.
61. D. L. Coleman, R. N. King and J. D. Andrade, *J. Biomed. Mater. Res.*, 1974, **8**, 199-211.
62. L. Marion, E. Haugen and I. A. Mjör, *J. Biomed. Mater. Res.*, 1980, **14**, 343-357.
63. J. M. Anderson, *Cardiovasc. Pathol.*, 1993, **2**, 33-41.
64. O. Frank, G. Tsoukleri, I. Riaz, K. Papagelis, J. Parthenios, A. C. Ferrari, A. K. Geim, K. S. Novoselov and C. Galiotis, *Nat. Commun.*, 2011, **2**, 255.

List of captions

Table 1 - Physical-chemical and morphological characteristics of p-CNTs and p,f-CNTs.

Table 2 - XPS elemental composition of the p-CNTs and p,f-CNTs samples.

Table 3 - Histological analysis of the tissue reactions associated with the subcutaneous implantation of p-CNT and p,f-CNT samples.

Fig. 1 - (a) Schematic image of the catalyst-supported CVD growth method of CNTs. (b-g) Photographs and respective SEM micrographs of the key steps of the preparation route of CNT membranes: (b,c) as-grown vertically aligned CNTs; (d,e) frieze-dried CNTs; (f,g) CNT membranes.

Fig. 2 - (a) Sketch of the doubly functionalized CNTs showing the aromatic chain (hydrophobic group, at green color) and the carboxylic groups (hydrophilic groups, at orange color). (b and c) STEM images of the p-CNTs and p,f-CNTs samples. (c and d) Respective HRTEM images of (b and c).

Fig. 3 - XPS analyses of the p-CNTs and p,f-CNTs samples: (a) survey spectra; (b) High resolution spectra and fitting curves of the C1s and O1s bands.

Fig. 4 - (a and b) SEM images showing the topography of the p-CNTs and p,f-CNTs samples. (c) High resolution image of the nano-rough CNT network (smooth area) of p,f-CNT sample.

Fig. 5 - Behaviour of MG63 osteoblastic cells over p-CNTs and *p,f*-CNTs membranes cultured for 1 and 4 days: (a) CLSM images of cells stained for F-actin cytoskeleton (green) and nucleus (red) and SEM images; (b) cell viability/proliferation (MTT assay), LDH leakage and ALP activity. Cultures performed on standard tissue culture plates were used as control. ●Significantly different from control; ♦ Significantly different from *p*-CNTs. Values of $p \leq 0.05$ were considered statistically significant.

Fig. 6 - Hematoxylin and eosin-stained sections of subcutaneous implanted membranes in Wistar rats, at 7 and 49 days post-operatively: (a-d) low magnification micrographs; (e-h) high magnification micrographs at 49 days (CNTs ropes highlighted by red arrows and individualized CNTs by a dotted red circle).

Fig. 7 - Optical images of the implanted (a) p-CNT and (b) p,f-CNT membranes with respective magnified images of the acquisition area of the Raman analysis as inset. (c and d) μ-Raman spectra of the materials of (a) and (b) for implanted times of 0, 7 and 49 days. (e and f) Respective integral intensities and FWHM measurements of the D- and G-bands of the Raman data of (c) and (d).

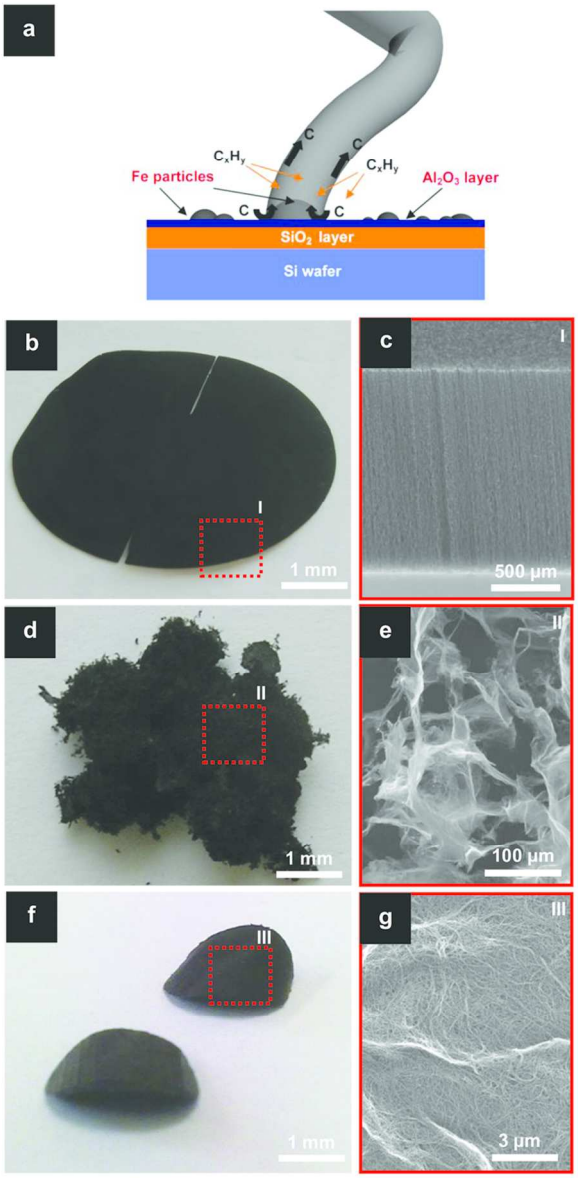

82x164mm (300 x 300 DPI)

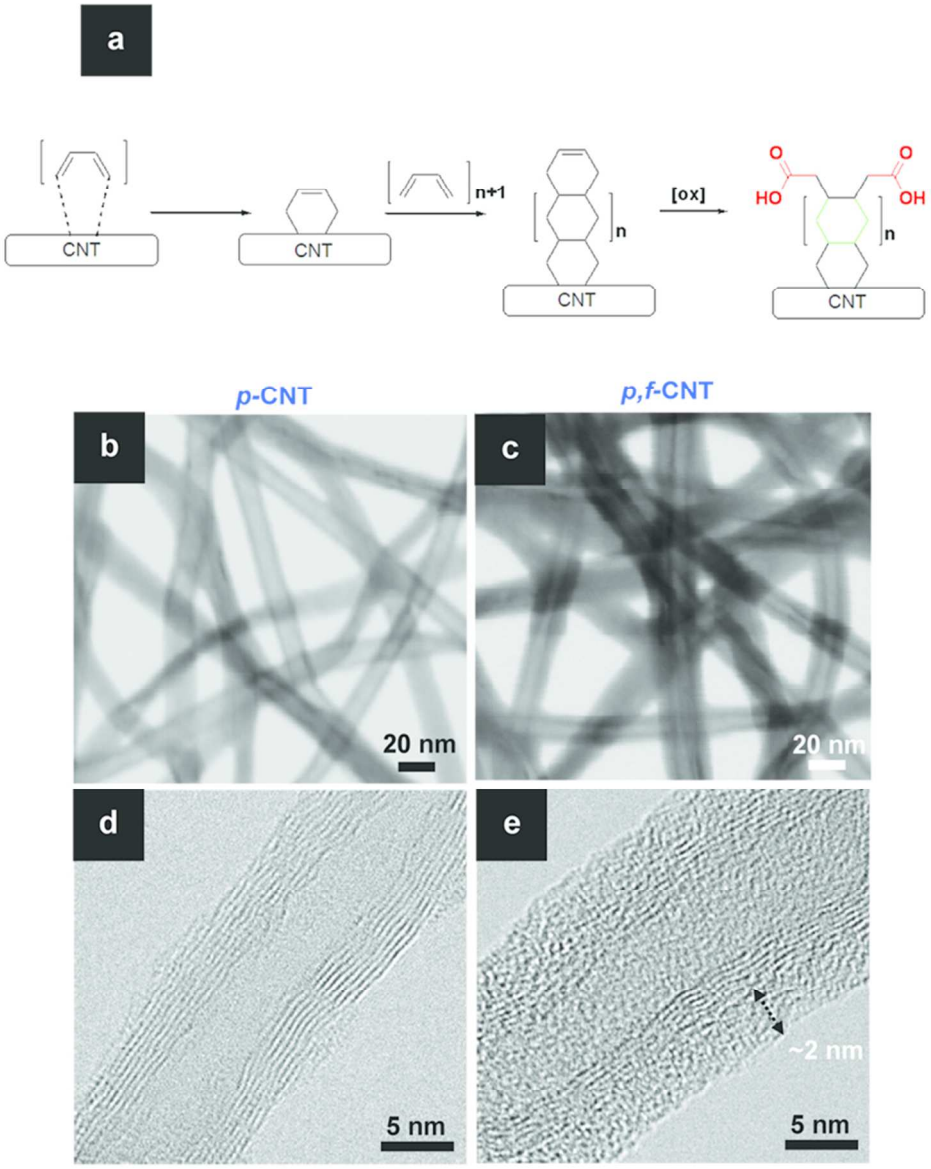

82x101mm (300 x 300 DPI)

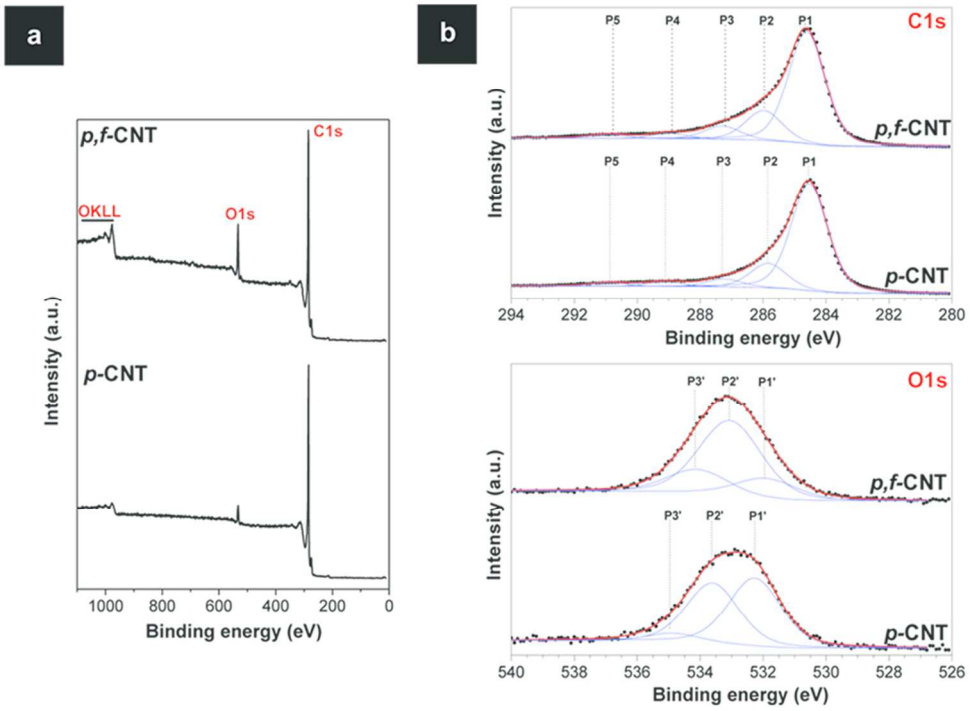

82x60mm (300 x 300 DPI)

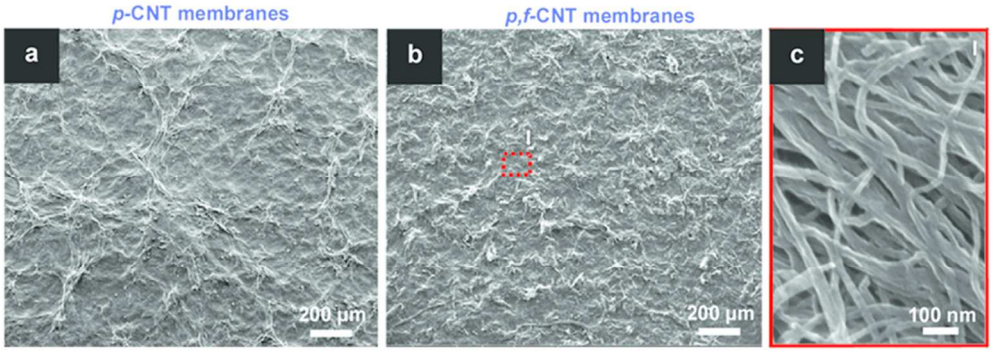

82x29mm (300 x 300 DPI)

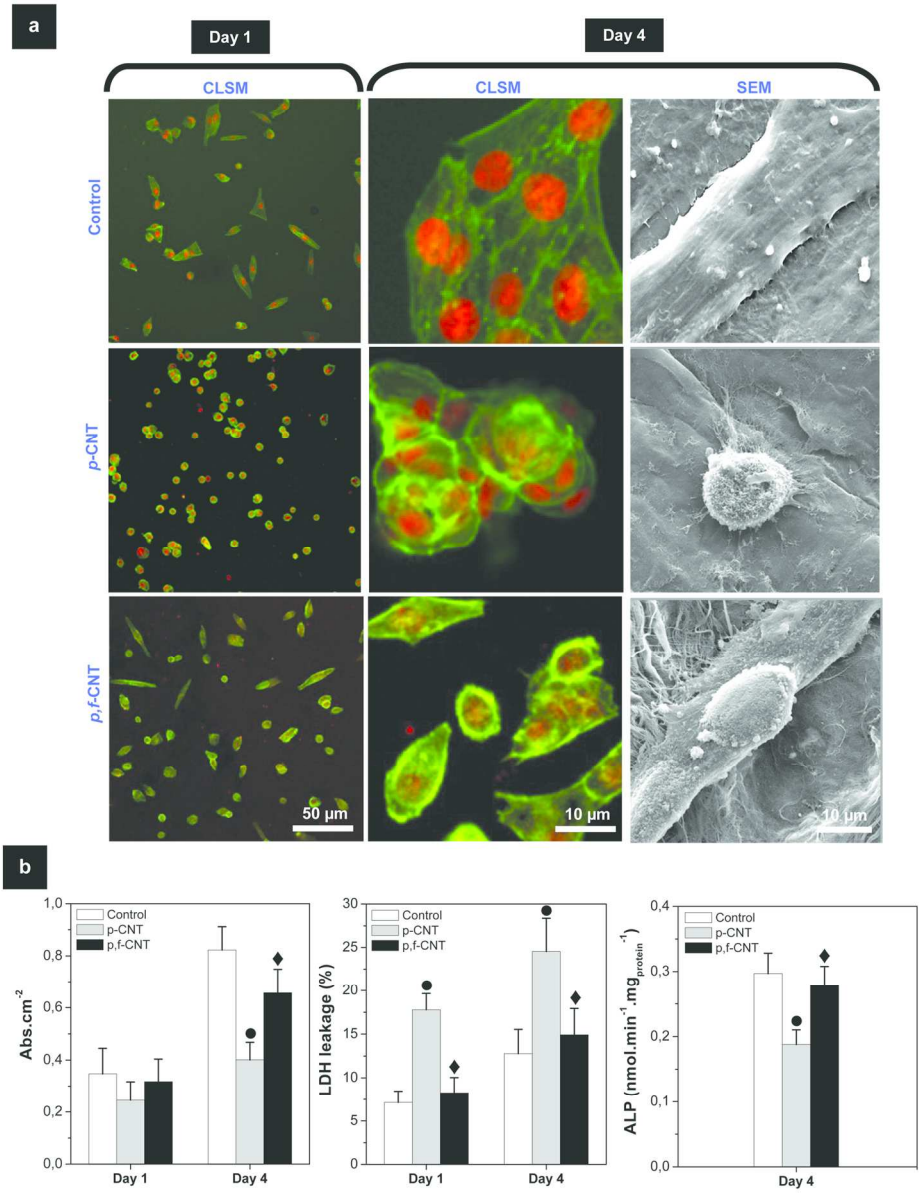

150x194mm (300 x 300 DPI)

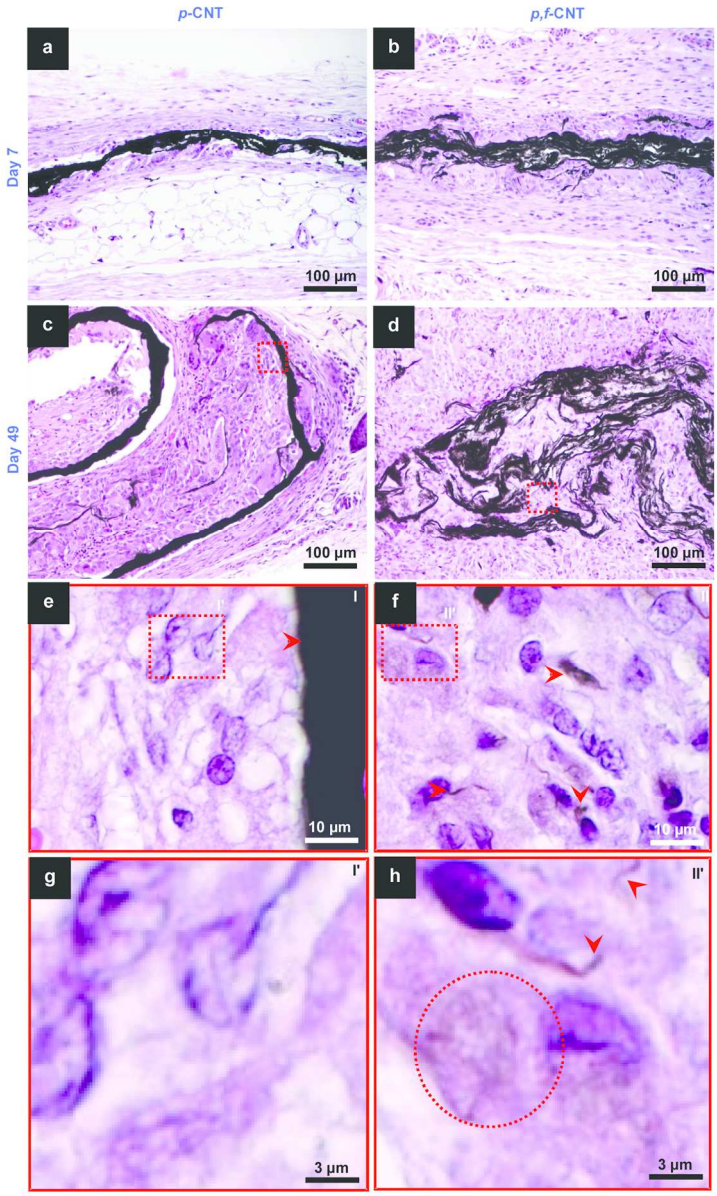

140x233mm (300 x 300 DPI)

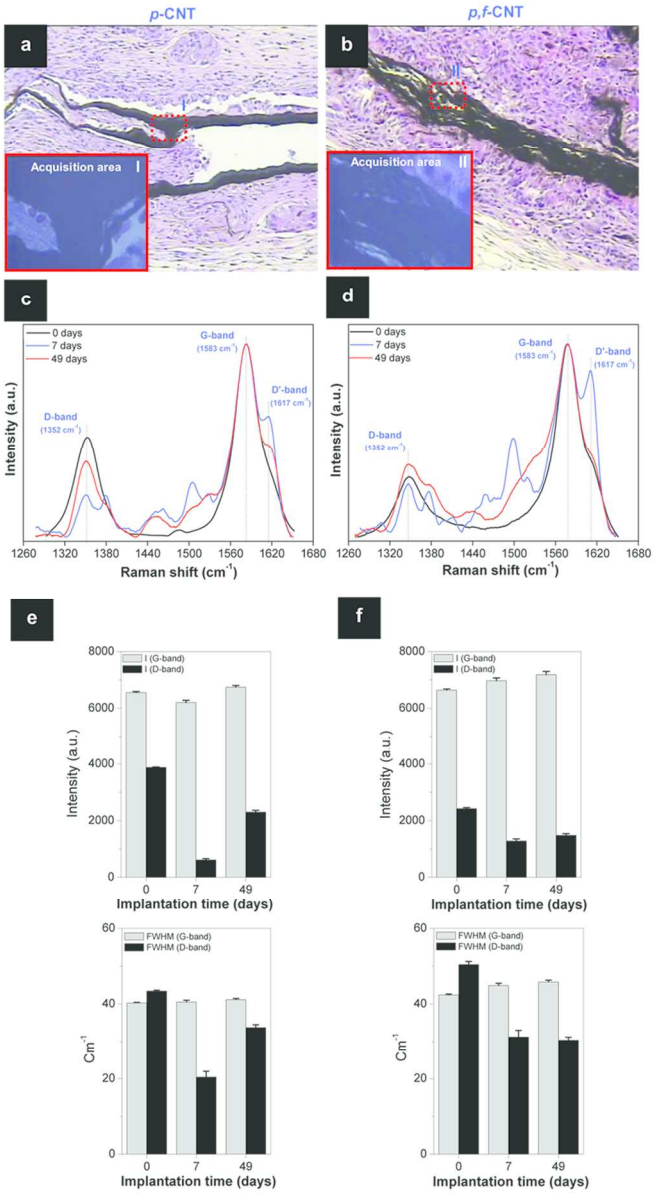

82x148mm (300 x 300 DPI)

Sample	Structural cristallinity L_a (nm)	Electrical conductivity ($S.m^{-1}$)	Surface area ($m^2.g^{-1}$)	Zeta potential (mV)	Contact angle (°)	Surface roughness S_a (µm)	Peak counts R_{Pc} ($peaks.mm^{-1}$)
p-CNT	31±1	$1x10^4±1x10^3$	203±9	-34±4	135±4	2.03±0.05	5±1
p,f-CNT	36±6	$3x10^3±9x10^2$	122±3	-50±5	123±3	1.47±0.03	9±1
p- purified *f*- functionalized							

150x27mm (300 x 300 DPI)

Samples	C1s (%)					O1s (%)			O:C
	P1	P2	P3	P4	P5	P1'	P2'	P3'	
p-CNT	71.4 (284.6eV)	18 (285.8eV)	5.1 (287.3eV)	3.0 (289.1eV)	2.5 (290.9eV)	46.1 (532.3eV)	45.6 (533.6eV)	8.3 (534.8eV)	0.045
p,f-CNT	68.2 (284.6eV)	18.5 (286eV)	7.5 (287.3eV)	3.3 (288.9eV)	2.5 (290.9eV)	14.6 (531.9eV)	62.6 (533.1eV)	22.8 (534.1eV)	0.093

109x18mm (300 x 300 DPI)

Timeframe	Sample	Thickness (μm)[a]	MØ[b]	Giant cells[b]	Lymphocytes[b]	Degradation[b]
Day 7	p-CNT	35-90	1	2	1	0/1
	p,f-CNT	44-133	2	2	1	1/2
Day 21	p-CNT	75-136	2	2	1	0/1
	p,f-CNT	105-166	3	3	1	2
Day 49	p-CNT	73-148	2	2	1	0/1
	p,f-CNT	172-250	3	3	2	3

[a]Minimum-Maximum
[b]Scoring system: 0-Absent; 1-Reduced; 2-Moderate; 3-Marked (adapted from Macleod et al., 2005)

109x31mm (300 x 300 DPI)